Economic Nonlinear Model Predictive Control of Prosumer District Heating Networks

Sibeijn, Max; Ahmed, Saeed; Khosravi, Mohammad; Keviczky, Tamas

DOI
10.1109/TCST.2025.3561501

Publication date
2025

Document Version
Final published version

Published in
IEEE Transactions on Control Systems Technology

Citation (APA)
Sibeijn, M., Ahmed, S., Khosravi, M., & Keviczky, T. (2025). Economic Nonlinear Model Predictive Control of Prosumer District Heating Networks. *IEEE Transactions on Control Systems Technology*, *33*(5), 1879-1894. https://doi.org/10.1109/TCST.2025.3561501

Economic Nonlinear Model Predictive Control of Prosumer District Heating Networks

Max Sibeijn, *Graduate Student Member, IEEE*, Saeed Ahmed, *Member, IEEE*, Mohammad Khosravi, *Member, IEEE*, and Tamás Keviczky, *Senior Member, IEEE*

***Abstract*—In this article, we propose an economic nonlinear model predictive control (MPC) algorithm for district heating networks (DHNs). The proposed method features prosumers, multiple producers, and storage systems, which are essential components of 4th-generation DHNs. These networks are characterized by their ability to optimize their operations, aiming to reduce supply temperatures, accommodate distributed heat sources, and leverage the flexibility provided by thermal inertia and storage—each crucial for achieving a fossil-fuel-free energy supply. Developing a smart energy management system to accomplish these goals requires detailed models of highly complex nonlinear systems and computational algorithms able to handle large-scale optimization problems. To address this, we introduce a graph-based optimization-oriented model that efficiently integrates distributed producers, prosumers, storage buffers, and bidirectional pipe flows, such that it can be implemented in a real-time MPC setting. Furthermore, we conducted several numerical experiments to evaluate the performance of the proposed algorithms in closed loop. Our findings demonstrate that the MPC methods achieved up to 9% cost improvement over traditional rule-based controllers while better maintaining system constraints.**

***Index Terms*—District heating networks (DHNs), economic model predictive control (MPC), large-scale systems, nonlinear MPC.**

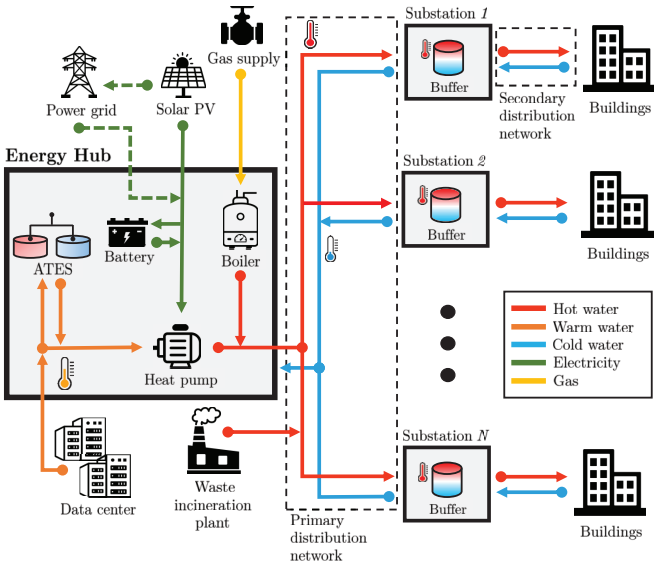

Fig. 1. Schematic of a DHN with multiple substations (consumers) and production points.

I. Introduction

THE energy transition requires a major shift from fossil fuel-based generation to renewable energy sources. In particular, the electrification of heat production is expected to grow enormously, see [1]. Given that the thermal energy sector contributes roughly 50% to the total final energy consumption within the EU [2], the need for sustainable heating becomes ever more substantial. Simultaneously, a global increase in the burden on power grids is evident, driven by rising electricity demand (e.g., heat pumps and electric vehicles) and fluctuating supply from renewables (e.g., wind and solar).

In order to address the higher demand and capacity limitations, a possible solution is to expand the existing infrastructure of power grids. However, expanding power grids is typically costly, time-consuming, and held back by a lack of appropriate regulatory frameworks [3]. An alternative solution is offered by the energy flexibility of district heating networks (DHNs). DHNs are networks of pipelines that transport heated water by circulating it around a district or city. Heat is either taken from or added to the network through heat exchangers located at consumers and producers, respectively. An example of a DHN is shown in Fig. 1.

The district heating offers numerous advantages. Economically, it is cost-effective to implement large installations that require less capacity due to simultaneous use. In addition, DHNs possess significant thermal inertia, allowing them to efficiently utilize free or inexpensive heat from industrial processes or underground geothermal sources. This characteristic provides DHNs with a synergistic element, often referred to as the economy of scope [4]. Moreover, DHNs can create and exploit flexibility on daily operational timescales by responding to market conditions, which can, in turn,

Received 30 January 2025; accepted 5 April 2025. Date of publication 2 May 2025; date of current version 20 August 2025. The work of Max Sibeijn and Tamás Keviczky was supported by the Local Inclusive Future Energy (LIFE) City Project, funded by the Ministry of Economic Affairs and Climate and by the Ministry of the Interior and Kingdom Relations of the Netherlands under Grant MOOI32019. The work of Saeed Ahmed was supported by the Dutch Research Council (NWO) under Grant ESI.2019.005. The work of Mohammad Khosravi was supported in part by the Swiss National Science Foundation (Postdoc.Mobility) under Grant 211104. Recommended by Associate Editor L. Imsland. *(Corresponding author: Max Sibeijn.)*

Max Sibeijn, Mohammad Khosravi, and Tamás Keviczky are with Delft Center for Systems and Control, Delft University of Technology, 2628 CN Delft, The Netherlands (e-mail: m.w.sibeijn@tudelft.nl; mohammad.khosravi@tudelft.nl; t.keviczky@tudelft.nl).

Saeed Ahmed is with the Jan C. Willems Center for Systems and Control, ENTEG, Faculty of Science and Engineering, University of Groningen, 9747 AG Groningen, The Netherlands (e-mail: s.ahmed@rug.nl).

Digital Object Identifier 10.1109/TCST.2025.3561501

alleviate strain on the electricity grid. Nevertheless, DHNs are large-scale systems with many distributed controllable assets. As a result, advanced control strategies are necessary for the effective operational management of these networks.

In the past, operational management of DHNs used rule-based controllers that set supply temperatures based on the outside temperatures [5], while mass flows were controlled locally at substations using simple tracking controllers. For the new generation of DHNs, referred to as *4th-generation district heating* [6], these control methods are insufficient. Several studies [5], [6], [7] emphasize the need for advanced control to achieve necessary goals, such as supply temperature minimization, creation of flexibility, distribution of heat generation, use of renewable energy sources, and fair sharing of heat. Closed-loop optimization-based control methods, such as model predictive control (MPC), are at the intersection of stabilizing control and operational optimization [8]. MPC combines the classical benefits of stabilizing control—such as robustness to demand prediction errors and model mismatch—with the advantages of optimization techniques. Therefore, MPC presents itself as a suitable and effective strategy for managing DHNs [7].

A. State of the Art

Classical control methods for DHNs relied on controlling the temperature and the differential pressure at central supply units. For details on these methods, we refer to [4] and [7], and the references therein. Recently, graph-based modeling techniques for DHNs have been a useful tool for developing various stabilizing controllers for both the hydraulic and thermal management of DHNs. In this context, the pressure and flow regulation problem was addressed in [9] and [10], temperature regulation was studied in [11] and [12], and the stabilizing control of both storage and temperature in a DHN was studied in [13], [14], and [15]. Moreover, the works [14], [15] introduced a multiproducer graph model integrating the dynamic evolution of storage volumes.

Operational optimization of DHNs has been a topic of interest for several decades, with earlier works dating back to the 1990s [16], [17]. These studies highlighted the complexity of managing load distribution while simultaneously minimizing supply temperatures, a challenge stemming from the nonlinear nature of thermal transients and their dependence on flow rates. Recent studies, such as [18], have addressed thermal transients and variable flow rates through the development of open-loop optimization-based controllers using graph-theoretic models based on partial differential equations (PDEs) governing the 1-D pipe dynamics. This work also employed a complementary constrained formulation, originating from the literature on gas transportation networks [19], to manage switching flow directions. However, the closed-loop implementation and important 4th-generation DHN features, such as multiple producers or storage, were not studied in [18].

Regarding MPC, the nonlinear nature of DHNs often complicates the design of a real-time implementable controller. Hence, several linearized formulations have been proposed, see [20], [21], [22], [23]. Recently, a nonlinear MPC and a mixed-integer nonlinear MPC were introduced for a small-scale network [24], [25], allowing the neglect of thermal transients to maintain a tractable formulation. Similarly, Frison et al. [26] developed an MPC algorithm for prosumer DHNs with storage, leaving out thermal transients and heat losses. While computationally attractive, disregarding thermal transients is not suitable for large-scale DHNs due to the significant time delays [16]. A nonlinear MPC scheme that considers thermal transients, multiple producers, and storage was considered in [27]. Nonetheless, a stabilizing scheme was employed instead of an economic scheme, the management of pressure and Kirchhoff loop constraints was not rigorously addressed, and prosumers were not included. Finally, La Bella et al. [28] developed a nonlinear MPC for the AROMA network, incorporating fixed-volume layered storage, as one subsystem within a multicarrier energy system. However, this work did not account for multiple producers, prosumers, or bidirectional flows.

While significant advancements have been made in the operational optimization and control of DHNs, current methods often lack consideration of essential features of 4th-generation DHNs, such as multiple producers, prosumers, bidirectional flows, and thermal transients. In addition, many approaches do not consider an economic objective or do not consider the complexity and scalability necessary to manage large-scale networks in real time. These gaps highlight the need for further research to develop comprehensive solutions that integrate these elements and address the computational challenges inherent in MPC for DHNs.

B. Contributions

In this work, we focus on the economic MPC of DHNs. Hence, we consider the problem of scheduling and management for economic operations. We state our contributions as follows.

1) We provide a control- and optimization-oriented, graph-theoretic model for DHNs that includes the following features: multiple producers, prosumers, storage, bidirectional pipe flow, thermal transients, adaptable model resolution, and a generalized Kirchhoff loop convexification approach that applies to DHNs with all previously mentioned features. We note that, to the best of the authors' knowledge, this is the first work to integrate all these features. In particular, we highlight the inclusion of prosumers, formerly only considered without thermal transients in [26], and the generalization of the Kirchhoff loop convexification approach, previously limited to single-producer DHNs [29].
2) We introduce a novel economic nonlinear MPC algorithm for DHNs and we provide numerical analysis of the convergence properties of the proposed controller.
3) We conduct a comprehensive study into the numerical performance of the proposed control methods in a closed-loop setting, specifically examining the added value of incorporating storage and multiple producers. In addition, we provide an in-depth analysis of the computational efficiency of our algorithms.

This article is structured as follows. In Section II, we introduce our general approach used to model DHNs. The following two sections are dedicated to specific modeling techniques for the hydraulic system (Section III) and the thermal system (Section IV). In Section V, we formulate the economic MPC problem and discuss the practical and theoretical convergence properties of the closed-loop system. Finally, Section VI contains the simulation results.

II. DHN Model

In this section, we detail the fundamental modeling choices and conventions, certain parts of which have been introduced in earlier work by Sibeijn et al. [30]. First, we define the graph-theoretic notions used to model the DHN in Section II-A. Subsequently, we discuss the transient thermal dynamics of pipe flow in Section II-B, and conservation constraints that are enforced through nodes in Section II-C. Finally, we introduce an example DHN called the AROMA network in Section II-D.

The modeling framework builds upon a fundamental characteristic of DHNs: their symmetric structure consisting of parallel supply and return pipelines. The supply network delivers hot water from heat sources to consumers, while the mirrored return network carries the cooled water back for reheating. This configuration enables cost-effective installation through shared infrastructure while supporting various pipe arrangements for efficient heat distribution [31], [32].

A. Graph Model

The DHN consists of hydraulic and thermal components such as pipes, junctions, pumps, valves, heat exchangers, and buffers. We model this network as a strongly connected directed graph $\mathcal{G} = (\mathcal{N}, \mathcal{E})$ with a set of nodes $\mathcal{N}$ that represent junctions in the DHN, which are connected by edges $\mathcal{E} \subseteq \mathcal{N} \times \mathcal{N}$, representing pipelines that may be fit with pumps, valves, or heat exchangers. Note that strong connectivity of $\mathcal{G}$ ensures no mass exits the system.

For the ease of discussion, let $\mathcal{N}$ be characterized as $\mathcal{N} := \{1, 2, \ldots, |\mathcal{N}|\}$. The *adjacency matrix* $D \in \{0,1\}^{|\mathcal{N}|\times|\mathcal{N}|}$ of $\mathcal{G}$ describes node-to-node connections, i.e., for any $(i, j) \in \mathcal{N} \times \mathcal{N}$, we have

$$D_{ij} = \begin{cases} 1, & \text{if } (i,j) \in \mathcal{E} \\ 0, & \text{otherwise.} \end{cases} \tag{1}$$

Given an enumeration for the edges of the graph modeling our DHN, the *incidence matrix* $E \in \{-1, 0, 1\}^{|\mathcal{N}|\times|\mathcal{E}|}$ of $\mathcal{G}$ describes the edge-to-node relationship, i.e., for any $(i, k) \in \mathcal{N} \times \{1, 2, \ldots, |\mathcal{E}|\}$, we have

$$E_{ik} = \begin{cases} -1, & \text{if the } k\text{th edge exits node } i \\ 1, & \text{if the } k\text{th edge enters node } i \\ 0, & \text{otherwise.} \end{cases} \tag{2}$$

In our model of the DHN, nodes correspond to volumeless junctions and edges correspond to pipes that may be equipped with heat exchangers, valves, or pumps [15]. On the other hand, for the sake of simplicity, we consider storage to consist of a fixed volume set of pipe segments, as used in [28], rather than the varying volume approach adopted by Machado et al. [15]. Consequently, the dynamic evolution of pressure and temperature within junctions reduces to algebraic equations, with pressure and temperature behavior fully determined by the edge dynamics.

B. Edge Dynamics

We model the dynamics of an edge representing a pipe, potentially equipped with a heat exchanger, pump, or a valve, through an approximation of the 1-D compressible Euler equations and the thermal energy equation for cylindrical pipes [18], [33]. Hence, the dynamics of edge $e \in \mathcal{E}$ are described through the following PDEs:

$$\partial_t \rho_e + \partial_x(\rho_e v_e) = 0 \tag{3}$$

$$\partial_t(\rho_e v_e) + \partial_x(\rho_e v_e^2) + \partial_x p_e + \rho_e g \hat{z}_e + K_e \frac{\rho_e}{2d_e} |v_e| v_e = 0 \tag{4}$$

$$\partial_t T_e + v_e \partial_x T_e + \frac{p_e}{\rho_e c_p} \partial_x v_e - \frac{K_e}{2c_p d_e} |v_e| v_e^2 + \frac{4U_e}{\rho_e c_p d_e} (T_e - T_a) = 0 \tag{5}$$

which are essentially characterizing the temporal and spatial evolution of three central variables; *temperature* $T_e(t, x)$ [K], *flow velocity* $v_e(t, x)$ [$\mathrm{m} \cdot \mathrm{s}^{-1}$], and *pressure* $p_e(t, x)$ [Pa] of water. The other parameters are the density of water ρ_e [$\mathrm{kg} \cdot \mathrm{m}^{-3}$], gravity g [$\mathrm{m} \cdot \mathrm{s}^{-2}$], slope of pipe $\hat{z}_e$ [-], friction coefficient K_e [-], diameter of pipe d_e [m], heat transfer coefficient U_e [$\mathrm{J} \cdot \mathrm{m}^{-2}\mathrm{K}^{-1}$], specific heat capacity of water c_p [$\mathrm{J} \cdot \mathrm{kg}^{-1}\mathrm{K}^{-1}$], and ambient temperature T_a [K].

Concerning the dynamics of DHNs, it is commonly assumed [18], [33] that the water inside the system is incompressible and has constant density, i.e., we have $\partial_x v_e = 0$, $\partial_t \rho_e = 0$, and $\partial_x \rho_e = 0$, for each $e \in \mathcal{E}$. Moreover, heat generated through friction is negligible in practice [33], particularly compared to other terms in (5). Therefore, we omit the term $(K_e/2c_p d_e)|v_e|v_e^2$ from (5). Moreover, since pipelines are typically laid underground at constant depth [32], we assume no elevation differences throughout the network, i.e., $\hat{z}_e = 0$, $\forall\, e \in \mathcal{E}$. In addition, considering the significant separation in time scales between thermal and hydraulic dynamics, and since the frictional term in (4) dominates the inertial term [34], one can neglect dynamics on the flow rate, i.e., $\partial_t v_e = 0$, for any $e \in \mathcal{E}$. Thus, for the dynamics of edge $e \in \mathcal{E}$, we have the following equations:

$$\partial_x p_e + K_e \frac{\rho}{2d_e} |v_e| v_e = 0 \tag{6}$$

$$\partial_t T_e + v_e \partial_x T_e + \frac{4U_e}{\rho c_p d_e} (T_e - T_a) = 0. \tag{7}$$

C. Nodal Constraints

The nodal constraints follow from conservation laws. At each network node, the conservation of mass principle combined with the incompressibility assumption requires that the total volumetric flow rate entering the node equals the total volumetric flow rate exiting the node. More precisely, for any node $n \in \mathcal{N}$, we define the edge sets $\mathcal{E}_{\to n} = \{e \in \mathcal{E} : e \text{ enters } n\}$

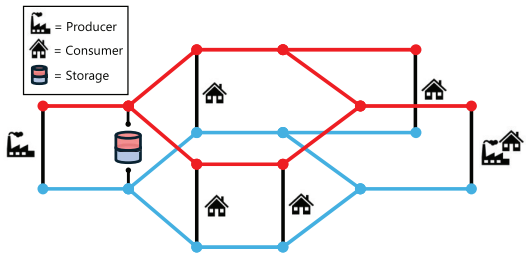

Fig. 2. AROMA DHN with multiple consumers, a prosumer, a storage buffer, and a loop.

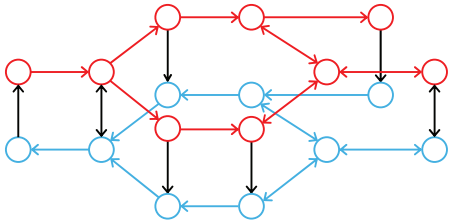

Fig. 3. Directed graph abstraction of the AROMA DHN with fixed flow directions. Double-sided arrows indicate the two opposite-facing edges.

and $\mathcal{E}_{n\rightarrow} = \{e \in \mathcal{E} : e \text{ exits } n\}$ as the set of entering and exiting edges, respectively. Subsequently, we obtain

$$\sum_{e\in\mathcal{E}_{\rightarrow n}} q_e(t) = \sum_{e\in\mathcal{E}_{n\rightarrow}} q_e(t) \tag{8}$$

where $q_e(t) = \Phi_e v_e(t)$ is the flow rate in pipe e with Φ_e the cross section of pipe. In addition, energy balance should also be considered for any node, which can be described as a mixing rule determining the relationship between the exit temperature of a node as a function of temperatures of entering flows. Accordingly, one can employ a mixing rule that takes a flow-weighted average of the incoming temperatures, as in [15] and [18], to obtain the temperature of a node. More precisely, for the temperature of any node $n \in \mathcal{N}$, we have

$$T_n(t) = \frac{\sum_{e\in\mathcal{E}_{\rightarrow n}} q_e(t)T_e(t)}{\sum_{e\in\mathcal{E}_{\rightarrow n}} q_e(t)} \tag{9}$$

Also, the temperature of any edge exiting a node is expected to be the same as the node temperature, i.e., we have

$$T_e(t) = T_n(t) \qquad \forall\, n \in \mathcal{N}\ \forall\, e \in \mathcal{E}_{n\rightarrow}. \tag{10}$$

The equations presented so far give rise to a graph theoretical model for DHNs. Thus, the system is described through a set of partial differential-algebraic equations (PDAEs), namely, (6)–(10), which is used as the base formulation for our future derivation in this article. It is worth noting the DHN model in the current form is not applicable for optimization purposes mainly due to the complex infinite-dimensional nature of the mentioned PDAEs. Accordingly, in Sections III and IV, we develop more tractable and yet realistic models, suitable for optimization-based control strategies.

D. AROMA: A Benchmark for DHNs

Before proceeding, we introduce the AROMA DHN, which is widely used in the DHN literature as a benchmark example to evaluate the performance of numerical algorithms, see [18], [28]. Therefore, we will employ this network to demonstrate the methodology developed in this article. The network, depicted in Fig. 2, features multiple consumers, producers, and a storage unit. Originally, the AROMA network consisted of only a single producer without any storage included [18]. Recently [28], storage was featured in the network by augmenting the AROMA network model. Considering that we are focused on the general case of DHNs, namely, with multiple producers/prosumers, for the demonstration of the proposed modeling scheme and the numerical validation of the developed methodology in this article, we additionally augment the AROMA DHN to accommodate the mentioned extensions and features. Nevertheless, one should note that our methodologies are applicable beyond the AROMA network.

III. DHN Model: A Tractable Reformulation for the Hydraulics

In this section, we improve the tractability of the DHN model introduced in Section II, with a particular focus on the hydraulic dynamics described by (6) and (8). To this end, we first introduce a new graph to accommodate bidirectional flows. Second, we describe the method used to compute a set of independent cycles that fully describe the mass flowing through the network. Third, we address the treatment of the momentum equation and introduce a convex reformulation for these constraints.

A. Fixing the Flow Direction

Considering the graph abstraction of a DHN as shown in Fig. 2, each pipeline is represented by a string of edges connected in series. Thus, in the coarsest representation of our system, we have exactly one edge for each pipeline until it reaches a junction. Hence, we have $|\mathcal{E}|$ pipelines, where with respect to each $e \in \mathcal{E}$, we define flow variables q_e that belong to the interval $\mathcal{Q}_e := \{q_e : \underline{q}_e \le q_e \le \overline{q}_e\}$, where $\overline{q}_e > 0$.

While seemingly a relatively minor detail, allowing the direction of the flow to switch during the operational phase has significant implications for the modeling procedure and complicates the design of a tractable controller. Therefore, for the edges where directional switching is allowed, i.e., for $e \in \mathcal{E}$ with $\underline{q}_e < 0$ and $\overline{q}_e > 0$, we decompose the corresponding flow variable as follows:

$$q_e = q_e^+ - q_e^-, \quad \text{with } q_e^+, q_e^- \ge 0, \text{ and } q_e^+ q_e^- = 0. \tag{11}$$

In terms of the graph, we obtain a new graph $\mathcal{G}^+ = (\mathcal{N}, \mathcal{E}^+)$ with additional set of edges $\mathcal{E}^+ = \mathcal{E} \cup \Delta_{\mathcal{E}}$, where $\Delta_{\mathcal{E}} := \{(v,u) \notin \mathcal{E} \mid e = (u,v) \in \mathcal{E} \text{ and } \underline{q}_e < 0\}$. To illustrate, we depict $\mathcal{G}^+$ for the AROMA network in Fig. 3. Here, $\mathcal{G}^+$ is directed, and double-sided arrows indicate pipelines that allow bidirectional flow. The direction matching the original orientation in $\mathcal{G}$ will have the flow q_e^+ associated with it, while the newly added reverse edge has q_e^- associated with it.

Remark 1: In typical DHNs, bidirectional flow is neither necessary nor practical for all pipeline segments. However, the bidirectional flow capability is essential for enabling prosumer

operation in the network. The determination of flow directionality is made during the design phase through the systematic analysis of network architecture. Therefore, not all edges in Fig. 3 are bidirectional. ◇

B. Independent Flows

We denote the vector of edge flow rates as $q = [q_e]_{e\in\mathcal{E}^+}$. The flow on an edge depends linearly on the flow on all other edges in the network due to the conservation of mass. As a result, we can reduce the number of free flow variables that we need to optimize for. To this end, we introduce the *reduced loop matrix* F_r which maps the reduced flow vector $q_r \in \mathbb{R}_+^{m_r}$ to q through

$$q = F_r^\top q_r \tag{12}$$

with $m_r < |\mathcal{E}^+|$. Intuitively, the vector q_r represents the flow that circulates the network, meaning that it passes through a supply section and its mirrored return section reaching back to its starting point. In the process, these flows pass through producers, consumers, or storage. In addition, we introduce the *fundamental loop matrix* F which maps all fundamental flows $q_f \in \mathbb{R}^{m_f}$ to q, i.e.,

$$q = F^\top q_f \tag{13}$$

with $m_f \leq m_r$. The vector q_f depends linearly on the elements of q_r. The matrices F_r and F consist of columns that describe directed cycles within $\mathcal{G}^+$. Nonetheless, F is a full column rank while F_r may not be. Similarly, q_r is a vector in the positive orthant, whereas the entries of q_f are not required to be nonnegative. The reason for introducing both F_r and F is that the nonnegativity of q_r in (12) significantly improves the numerical results compared to using (13), while F is primarily employed for theoretical purposes, as further detailed in Section III-D.

In [9], a method is presented to compute the fundamental loop matrix F by setting the free flow variables as they flow through the chords of the spanning tree of $\mathcal{G}$. Consequently, a fundamental loop is defined as the loop that is formed whenever a chord is reconnected to the spanning tree. Then, the fundamental loop matrix F has elements $F_{ij} \in \{-1, 0, 1\}$, for all i and j, depending on the orientation of the chord and whether an edge is part of a fundamental loop.

To preserve the nonnegativity of all elements in F, we develop a slightly different approach to compute F. To this end, we need the notion of a *directed cycle* [35].

Definition 1 (Directed Cycle) A directed cycle $\mathcal{C}$ in $\mathcal{G}$ is a sequence of nodes and edges as $(n_0, e_1, n_1, e_2, \ldots, e_k, n_k)$ such that the following hold.

1) $n_0, n_1, \ldots, n_k$ are different nodes.
2) $e_i = (n_{i-1}, n_i)$ for $i = 1, \ldots, k$.
3) $n_0 = n_k$.

where two sequences are an equivalent cycle if one can be obtained from the other by a cyclic permutation.

Let $\mathcal{S}(\mathcal{G}) := \{\mathcal{C}_i(\mathcal{G})\}$ be the set of all directed cycles within $\mathcal{G}$. The matrices F_r and F can be computed through the following procedure.

1) Compute all directed cycles $\mathcal{S}(\mathcal{G}^+)$ in $\mathcal{G}^+$.
2) Remove any cycles that consist of at most two nodes.
3) Remove any asymmetric cycles, i.e., cycles for which their path is not mirrored between the supply and return network. We call this reduced set $\mathcal{S}_r(\mathcal{G}^+)$.
4) Define reduced loop matrix F_r with elements

$$F_{r,ij} = \begin{cases} 1, & \text{if edge } j \in \mathcal{C}_i \text{and cycle } \mathcal{C}_i \in \mathcal{S}_r\left(\mathcal{G}^+\right) \\ 0, & \text{otherwise} \end{cases}$$

where F_r has $m_r = |\mathcal{S}_r(\mathcal{G}^+)|$ rows and $|\mathcal{E}^+|$ columns.
5) Compute F by performing a pivoted QR factorization on $F_r^\top$ as follows:

$$F_r^\top P = QR \tag{14}$$

where $R \in \mathbb{R}^{|\mathcal{E}^+|\times m_r}$ is an upper triangular matrix, $Q \in \mathbb{R}^{|\mathcal{E}^+|\times|\mathcal{E}^+|}$ is an orthonormal matrix, $P \in \mathbb{R}^{m_r\times m_r}$ is a permutation matrix, and the columns of $F_r^\top P$ are projected onto an orthonormal basis spanned by the columns of Q. If $\text{rank}(F_r) = m_f < m_r$, all elements R_{ii} with $i > m_f$ are 0, indicating that corresponding columns of $F_r^\top P$ lie in the subspace of all prior columns. Hence, we obtain the fundamental loop matrix by taking only the first m_f columns of $F_r^\top P$ as follows:

$$F = \left(F_r^\top P \begin{bmatrix} I_{m_f} \\ \mathbf{0} \end{bmatrix}\right)^\top. \tag{15}$$

The set of remaining cycles is denoted by $\mathcal{S}_f(\mathcal{G}^+)$.

Matrix F, constructed via QR factorization with column pivoting on $F_r^\top$, inherits nonnegativity from F_r and possesses full column rank, ensuring mass conservation within the network.

Remark 2: We note that, in principle, the rows of the computed fundamental loop matrix span the same basis as the row space of the matrices introduced in [9] and [15]. The only difference is that, in this context, we exclude asymmetric cycles without the loss of generality. ◇

C. Treatment of the Momentum Equation

In practice, due to the significant time scale separation between the hydraulic and thermal dynamics, the control of corresponding components within the DHN is executed over different time intervals. Thus, the dynamic behavior of flows and pressure throughout the network is less of a concern here. Nonetheless, one needs to certify the feasibility of the hydraulic operation. More precisely, we want to identify a set $\mathcal{Q}$, such that for all $q \in \mathcal{Q}$, pressure remains within the limits at all nodes of the network, and Kirchhoff's second law, stating that the sum of pressure differences along each loop in the network equate to 0, is satisfied.

One can approximate the conservation of momentum equation (6) by substituting v_e with $v_e = (4q_e/\pi d_e^2)$ and discretizing $\partial_x p = (\Delta p_e/L_e)$, where L_e denotes the pipe length, for each $e \in \mathcal{E}^+$. Accordingly, one obtains the equation describing pressure drop over pipe segment e caused by friction as follows:

$$\Delta p_e = 8\rho L_e \frac{K_e}{\pi^2 d_e^5}|q_e|q_e = R_{\mu,e}q_e^2 \quad \forall\, e \in \mathcal{E}^+ \tag{16}$$

where $R_{\mu,e}$ is a combined constant term representing the frictional resistance in the pipe. Additionally, the sign dependency

for q_e is removed according to (11), i.e., the flow direction on each edge is fixed.

We define the sets $\mathcal{P} \subset \mathcal{E}^+$ and $\mathcal{V} \subset \mathcal{E}^+$ that contain the edges with a pump and a valve, respectively. Then, for each edge $e \in \mathcal{P}$, the pressure change over e is described by

$$\Delta p_e = R_{\mu,e} q_e^2 - h_e(r_e) \tag{17}$$

with $h_e(r_e) = c_e r_e$ being the pressure difference induced by the pump, c_e being the maximum pumping power capacity, and $r_e \in [0, 1]$ being the normalized pump speed. In addition, for each edge $e \in \mathcal{V}$, the pressure drop over e is described by

$$\Delta p_e = R_{\mu,e} q_e^2 + R_{v,e}(v_e) q_e^2 \tag{18}$$

where $0 \leq R_{v,e}(v_e) < \infty$ is a time-varying control variable and $v_e \in [0, \infty)$ is the position of the valve such that $R_{v,e}(0) = 0$ corresponds to the full opening of the valve and $\lim_{v_e \to \infty} R_{v,e}(v_e) \to \infty$ corresponds to the full closing of the valve. Here, we are not considering specific valve types and characteristics. It is sufficient to only assume that any increase in v_e will increase the resistance over the valve such that $R_{v,e}$ is strictly monotone. Nonetheless, for ease of discussion, one can consider $R_{v,e}$ to be linear in $v_e \in [0, \infty)$, i.e., we have $R_{v,e}(v_e) = R_{v,e} v_e$, where $R_{v,e}$ is a positive scalar indicating the resistance coefficient of the valve.

D. Convex Reformulation of the Kirchhoff Loop Constraints

The constraints imposed by (16)–(18) are nonconvex with respect to the flow rate due to the quadratic friction terms, and therefore, they need to be reformulated. More precisely, defining $\mathcal{S}^\dagger(\mathcal{G}^+)$ as the set of *all* cycles in $\mathcal{G}^+$ independent of the direction of the edges, Kirchhoff's second law states that

$$\sum_{e \in \mathcal{C}_i} \Delta p_j = 0 \quad \forall \mathcal{C}_i \in \mathcal{S}^\dagger\left(\mathcal{G}^+\right) \tag{19}$$

i.e., for each cycle, we need to satisfy a quadratic equality constraint, which is essentially nonconvex.

The pressure is defined pointwise in space, and therefore, we consider a pressure variable p_n, for each $n \in \mathcal{N}$. Let $\mathbf{p}_n \in \mathbb{R}^{|\mathcal{N}|}$ be the vector of nodal pressures and $\Delta \mathbf{p}_e \in \mathbb{R}^{|\mathcal{E}^+|}$ be the vector of pressure differences over all edges. Combining (16)–(18), we have

$$-E^\top \mathbf{p}_n = \Delta \mathbf{p}_e = R(v)\,(q \odot q) - H(r) \tag{20}$$

where $\odot$ denotes the elementwise product of two vectors, $R(v) = R_\mu + R_v(v)$ is a diagonal matrix that has on its diagonal the sum of resistances due to friction and valve effects on each edge, and $H(r)$ is the vector of induced pump pressure difference for each edge. As in [15], we multiply (20) from the left by F to obtain the sum of pressure difference overall fundamental cycles as follows:

$$-FE^\top \mathbf{p}_n = \sum_{e \in \mathcal{C}_i} \Delta p_e = 0 \quad \forall \mathcal{C}_i \in \mathcal{S}_f\left(\mathcal{G}^+\right). \tag{21}$$

Subsequently, combining (20) and (21) leads to

$$FR(v)(q \odot q) = FH(r) \tag{22}$$

implying that the sum of all pressure drops due to valve effects and friction in any directed cycle of the graph should be equal to the sum of all induced pump pressure differences within that same cycle. Similarly, we introduce the inequality

$$F_r R_\mu (q \odot q) \leq F_r H(\mathbf{1}) \tag{23}$$

where $\mathbf{1}$ denotes the vector of all ones, i.e., $\mathbf{1} = [1, \ldots, 1]^\top$. Equation (23) represents an upper bound on the induced pressure difference along each loop and corresponds to the scenario, where all valves are maximally open and all pumps are operated at maximum capacity, i.e., $v_e = 0$, $\forall\, e \in \mathcal{V}$, and $r_e = 1$, $\forall\, e \in \mathcal{P}$.

Before proceeding to the main result of this section, we need to introduce the following assumption.

Assumption 1: There are $|\mathcal{V}| \geq m_f$ edges with a valve placed throughout the network, and the position of these edges is such that $\operatorname{rank}(F\Pi) = m_f$, where $\Pi \in \{0, 1\}^{|\mathcal{E}^+| \times |\mathcal{V}|}$ is a selection matrix with entries

$$\Pi_{ek} = \begin{cases} 1, & \text{if valve } k \text{ is on edge } e \\ 0, & \text{otherwise} \end{cases}$$

for any $e \in \{1, 2, \ldots, |\mathcal{E}^+|\}$ and any $k \in \{1, 2, \ldots, |\mathcal{V}|\}$. Since $F\Pi$ is full row rank, it can be mapped back to F through a linear transformation, i.e., we have

$$F = F\Pi\Psi \tag{24}$$

where $\Psi = (F\Pi)^\dagger F$ and $(\cdot)^\dagger$ denotes the Moore-Penrose pseudoinverse. Let m_Θ be the dimension of the null space of matrix $F\Pi$. We assume that there exist matrices $Z_1, Z_2 \in \mathbb{R}^{m_\Theta \times |\mathcal{E}^+|}$ such that

$$(\Psi + \Theta_{F\Pi} Z_1)\, H(\mathbf{1}) \geq (\Psi + \Theta_{F\Pi} Z_2)\, R_\mu (q \odot q) \tag{25}$$

where $\Theta_{F\Pi} \coloneqq I - (F\Pi)^\dagger F\Pi$ denotes the kernel of $F\Pi$.

Before proceeding further, we need to highlight several remarks about the introduced assumption.

Remark 3: Multiplying (25) from the left by $F_r\Pi$ yields (23). In the majority of cases, the validity of (23) implies that (25) is also satisfied. Nonetheless, (25) can be explicitly guaranteed by imposing it as a constraint within the MPC formulation introduced in Section V. Note that, to ensure convexity, it may be required to determine Z_2 a priori such that $\Psi + \Theta_{F\Pi} Z_2$ is a matrix with nonnegative entries. ⋄

Remark 4: One can easily ensure the existence of matrix Z_2 such that the right-hand side of (25) is elementwise nonnegative. To this end, we need to consider only the supply section of the DHN. Then, the corresponding graph consists of source nodes coming from producers, sink nodes reaching consumers, and intermediate nodes that represent junctions. In addition, we consider networks where the degree of each intermediate node is at most three, meaning that each junction is either a *splitting node* or a *merging node*. Valves are positioned in reverse cascading order from consumers to intermediate nodes. At splitting nodes, valves are required on outgoing edges, except when an edge connects directly to another splitting node. For merging nodes, valve placement is only necessary on edges originating from producer nodes; otherwise, the analysis proceeds to the subsequent node. This process is repeated until all edges are traversed. We illustrate this procedure in Fig. 4. The rationale for this valve-checking strategy is that it ensures

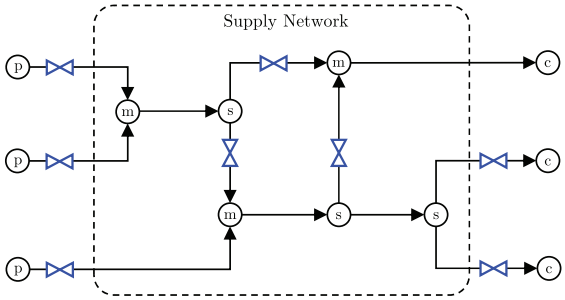

Fig. 4. Valve checking procedure, described in Remark 4, illustrated by showing the flow from producers (p) to consumers (c) going through the supply network consisting of merging nodes (m) and splitting nodes (s).

the flow on any edge lacking a valve becomes a nonnegative linear combination of the flows on edges equipped with valves. Formally, this implies the existence of a matrix $\Psi + \Theta_{F\Pi} Z_2$ with exclusively nonnegative entries. ◇

Remark to Practitioners: While the valve placement strategy may appear extensive, it reflects the fundamental requirement that a high degree of freedom in flow control requires a sufficiently high number of strategically placed pumps or valves. In practical situations, where valve placement is restricted by physical or economic constraints, analyzing (25) helps determine where fewer valves can still preserve convexity. In cases where achieving convexity is not feasible, it serves as a practical tool for practitioners to uncover inherent system limitations. These insights can support the design phase by identifying the most impactful valve placements or guide the development of operational constraints that satisfy (25) within practical limitations. ◇

Remark 5: The valve placement approach described in Remark 4 extends naturally to networks with bidirectional edges, where nodes connect to edges that can experience flow in both directions are treated as both merging and splitting nodes to account for all operational modes. Nevertheless, for bidirectional edges, a single physical valve suffices since only one flow direction is active at any given time. Furthermore, one should note that the introduced assumption on the total number of required valves aligns with the literature on DHNs [9], [15], where each chord of the graph's spanning tree is equipped with a valve. ◇

The following proposition guarantees that (23) is a sufficient condition for (22).

Proposition 1: Let Assumption 1 hold. Then, for any q that satisfies (23), there exist $\nu \in \mathbb{R}_+^{|\mathcal{V}|}$ and $r \in [0,1]^{|\mathcal{P}|}$ such that (22) is satisfied.

Proof: Recall that, for any valve openings ν, we have $R(\nu) = R_\mu + R_\nu(\nu)$, where $R(\nu)$ is a diagonal matrix that has on its diagonal the sum of resistances due to friction and valve effects on each edge. Hence, we have

$$FR(\nu)(q \odot q) = FR_\mu(q \odot q) + FR_\nu(\nu)(q \odot q). \tag{26}$$

Furthermore, we know that, for any ν, q, and Π, there exists a positive semidefinite diagonal scaling matrix $D_{R,q}$ and a vector $y = D_{R,q}\nu$, where y represents a scaled substitute of the valve openings, such that we can write $R_\nu(\nu)(q \odot q) = \Pi y$. Therefore, we have

$$FR(\nu)(q \odot q) = FR_\mu(q \odot q) + F\Pi y. \tag{27}$$

Accordingly, to show that (22) holds for some y and r, we need to verify the same argument for the following equation:

$$FH(r) = FR_\mu(q \odot q) + F\Pi y. \tag{28}$$

If we set $r = \mathbf{1}$, then it is enough to show that there exists $y \in [0,\infty)^{|\mathcal{V}|}$ such that

$$F\Pi y = F\left(H(\mathbf{1}) - R_\mu(q \odot q)\right). \tag{29}$$

From (23), we have that the right-hand side of (29) is elementwise nonnegative, which is necessary for the existence of nonnegative solutions to y. Following Assumption 1, we know that (29) can be written as follows:

$$F\Pi\left(y - \Psi H(\mathbf{1}) + \Psi R_\mu(q \odot q)\right) = 0. \tag{30}$$

Hence, the solutions to (30) lie inside the null space of $F\Pi$. Accordingly, we know that, for each y satisfying (30), there exists $z \in \mathbb{R}^{m_\Theta}$ such that

$$\begin{aligned} y &= \Psi H(\mathbf{1}) - \Psi R_\mu(q \odot q) + \Theta_{F\Pi} z \\ &= (\Psi + \Theta_{F\Pi} Z_1) H(\mathbf{1}) - (\Psi + \Theta_{F\Pi} Z_2) R_\mu(q \odot q) \end{aligned} \tag{31}$$

where $Z_1, Z_2 \in \mathbb{R}^{m_\Theta \times |\mathcal{E}^+|}$ are the matrices introduced in Assumption 1. Thus, due to (25), we have that y is a vector with nonnegative entries, which implies that $\nu \geq 0$. More precisely, there exist $\nu \in \mathbb{R}_+^{|\mathcal{V}|}$ and $r \in [0,1]^{|\mathcal{P}|}$ such that (22) is satisfied. This concludes the proof. ■

The previous proposition guarantees, for any q satisfying (23), the existence of ν and r satisfying (22), and, therefore, satisfying (21). In the following proposition, we show that (21) implies (19), meaning that Kirchhoff's second law is fulfilled.

Proposition 2: Under Assumption 1, we have that (21) is a necessary and sufficient condition for (19), i.e., if there exists a (q, ν, r) such that (21) holds, then (19) is also satisfied.

Proof: Considering $\mathcal{S}_f \subseteq \mathcal{S}^\dagger$, from the definition of (19) and (21), we know that (19) implies (21). Therefore, we only need to prove the sufficiency part of the claim.

Let F_i be the ith row of F, i.e., F_i is a vector with elements equal to $F_{ij} = 1$ if $j \in \mathcal{C}_i$ and 0 otherwise. All cycles $\mathcal{C}_1, \mathcal{C}_2, \ldots, \mathcal{C}_{m_f}$ form a cycle basis for $\mathcal{G}^+$, which means that there are m_f linearly independent basis vectors $F_1, \ldots, F_{m_f}$ spanning the basis of all other cycles in the graph. As a result, any vector $F^{(\mathcal{C})}$, which corresponds to a cycle $\mathcal{C} \in \mathcal{S}^\dagger \setminus \mathcal{S}_f$, can be constructed by $F_1, \ldots, F_{m_f}$ as the following integer linear combination:

$$F^{(\mathcal{C})} = \sum_{i=1}^{m_f} a_i F_i \tag{32}$$

where $a_1, \ldots, a_{m_f} \in \mathbb{Z}$. Therefore, for the sum of pressure differences over $\mathcal{C}$, we have

$$\begin{aligned} \sum_{e \in \mathcal{C}} \Delta p_e &= F^{(\mathcal{C})} \Delta \mathbf{p}_e \\ &= \sum_{i=1}^{m_f} a_i F_i \Delta \mathbf{p}_e = \sum_{i=1}^{m_f} a_i \sum_{e \in \mathcal{C}_i} \Delta p_e. \end{aligned} \tag{33}$$

Subsequently, from (21), it is implied that

$$\sum_{e\in\mathcal{C}} \Delta p_e = 0 \tag{34}$$

which concludes the proof. ■

In the following proposition, we present the key result regarding the convexity of (23).

Proposition 3: Equation (23) is convex with respect to flow vectors q and q_r.

Proof: For $i = 1,\dots,m_f$, let matrix $\mathbf{R}_\mu^i$ be defined as follows:

$$\mathbf{R}_\mu^i = \operatorname{diag}(F_{r,i})R_\mu \tag{35}$$

which is a diagonal matrix with nonnegative entries, and thus, positive semidefinite. According to the definition of F_r, R_μ, and h_e, and (23), we have

$$q^\top \mathbf{R}_\mu^i q = \sum_{e\in\mathcal{C}_i} R_{\mu,e} q_e^2 \le \sum_{e\in\mathcal{C}_i} h_e(1) = \sum_{e\in\mathcal{C}_i} c_e \tag{36}$$

for any $i = 1,\dots,m_r$, which is equivalent to (23) and implies that it is convex with respect to q. For any $i = 1,\dots,m_r$, define matrix $\mathbf{Z}^i$ as follows:

$$\mathbf{Z}^i = F_r \mathbf{R}_\mu^i F_r^\top. \tag{37}$$

Note that the positive semidefiniteness of $\mathbf{R}_\mu^i$ implies the same property for $\mathbf{Z}^i$, for each $i = 1,\dots,m_r$. From $q = F_r^\top q_r$, one has

$$q_r^\top \mathbf{Z}^i q_r = \left(F_r^\top q_r\right)^\top \mathbf{R}_\mu^i \left(F_r^\top q_r\right) = q^\top \mathbf{R}_\mu^i q. \tag{38}$$

Accordingly, we can write (36), or equivalently (23), as follows:

$$q_r^\top \mathbf{Z}^i q_r \le \sum_{e\in\mathcal{C}_i} c_e \quad \forall i = 1,\dots,m_r \tag{39}$$

which implies the convexity of (23) with respect to q_r. This concludes the proof. ■

The proposed propositions indicate the presence of a convex reformulation of Kirchhoff's second law through (23). Proposition 1 shows that this reformulation ensures the existence of a feasible set of valve openings necessary to achieve the specified flow vector q. Moreover, Proposition 2 describes the sufficiency of (21) for satisfying (19). Finally, we demonstrate the convexity of (23) through a straightforward transformation as detailed in Proposition 3.

Remark 6: More generally, we expect the results to hold for other convex pressure-flow relationships, e.g., $\Delta p = \mathcal{R}_\mu(q)$, not just the quadratic one typical for turbulent flow in DHNs. When replacing (16) with such a function, the optimization problem preserves convexity, since the left-hand side of (23) remains a sum of convex functions. Since Propositions 1 and 2 are independent of the specific form of $\mathcal{R}_\mu(q)$, the arguments should still apply. ◇

IV. DHN Model: A Tractable Reformulation for the Thermal Dynamics

To obtain a tractable formulation for the thermal dynamics in the network, a suitable discrete spatial approximation of (7) is required, for which we apply an upwind scheme. Therefore, the dynamics of the ith finite volume cell of water can be described by the following scalar continuous-time ordinary differential equation (ODE):

$$\begin{aligned} V_i \dot{T}_i &= -q_i(T_i - T_{i-1}) - \alpha_i(T_i - T_a) + w_i \\ y_i &= q_i(T_i - T_a) \end{aligned} \tag{40}$$

where $V_i = \Phi_i \tau_{x_i}$ denotes the cell volume, q_i denotes the mass flow of water, T_i denotes the temperature of water in the cell, T_{i-1} is the temperature of the inflow into the cell, $\alpha_i = 4U_iV_i/\rho c_p d_i$ is the heat loss coefficient, T_a is the ambient temperature, w_i is a variable denoting the transfer of heat from or to the environment, and y_i is the output which is proportional to the exergy. Note that, similar to [15], when the cell represents a heat exchanger, w_i indicates the transfer of heat from one side to the other side, and otherwise, the term w_i can be dropped from (40). Hence, w_i is a control variable if it corresponds to a controllable producer, and a disturbance if it corresponds to an uncontrollable producer or consumer.

We define the state variable x_i as $x_i = T_i - T_a$, assuming that the ambient temperature is equal and constant for all cells, and consider the corresponding dynamics described as follows:

$$\begin{aligned} V_i \dot{x}_i &= -(q_i + \alpha_i)x_i + u_i + w_i \\ y_i &= q_i x_i. \end{aligned} \tag{41}$$

Note that (40) is equivalent to (41) when $u_i = q_i x_{i-1}$. From here on, we consider any finite volume cell as a node, or more precisely, a thermal node (TN), in the graph. The TN has a compartmental structure as shown in Fig. 5(a).

Remark 7: The energy transfer rate w_i and flow rate q_i in (41) appear decoupled at first glance, however, their relationship becomes evident under steady-state conditions ($V_i = 0$), where the energy balance shows that w_i increases with q_i, leading to greater heat transfer at higher flows. ◇

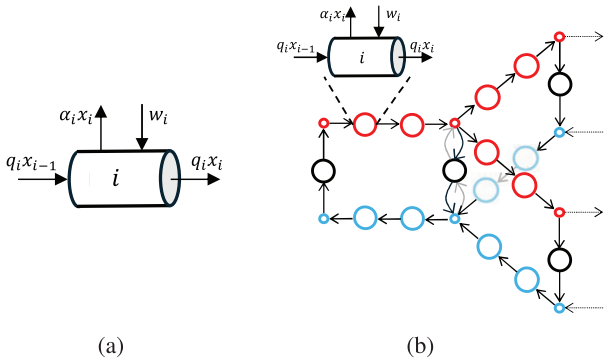

Fig. 5. Illustration of TN model and mesh refinement of the DHN graph. (a) Conceptual TN model with its dynamics defined by (41) and (b) injection of TNs in a refinement of the AROMA network.

A. State-Space Representation of the DHN Interconnection

To construct the model of the thermal system, we approximate the spatial evolution of temperature along pipelines, described by (7), through a finite sequence of partitions. We adopt an approach similar to [36], where nodes represent volumes of water and edges represent flow rates.

1) Updating the Graph: We introduce intermediate nodes on all edges of the original graph to increase the granularity of the model and improve the approximation of (7). These nodes follow the compartmental dynamics of (41), i.e., TNs. Given the original graph $\mathcal{G}^+ = (\mathcal{N}, \mathcal{E}^+)$ with adjacency matrix D^+, we add $l_{x,i}$ TNs to each edge i, creating $m_c = \sum_{i=1}^{|\mathcal{E}^+|} l_{x,i}$ total new nodes. The resulting augmented graph has adjacency matrix $\tilde{D}$ of dimension $|\mathcal{N}| + m_c$, as partially shown in Fig. 5(b). Further details and explanation on how to obtain $\tilde{D}$ are provided in [37].

Remark 8: The extension of the graph does not change the independent flow distribution in the network presented in Section III. Without the loss of generality and for the ease of notation, we use q to denote the extended mass flow variable. Nonetheless, considering the introduced graph augmentation, the precise definition of the flow variable in the new setting is $q = \left[q_i \otimes \mathbf{1}_{p_i}\right]_{i\in\mathcal{E}^+}$. ◇

2) From Graph to State Space: Let $\tilde{\mathcal{G}} = (\tilde{\mathcal{N}}, \tilde{\mathcal{E}})$ be the resulting graph with $|\tilde{\mathcal{N}}| = |\mathcal{N}|+m_c$ nodes and incidence matrix $\tilde{E}$, where $|\mathcal{N}|$ and m_c denote the number of junctions and TNs, respectively. To model energy flow rates between nodes, we define edge variable $\varphi_e(q_e, x_e) = q_e x_e$, which requires the root node temperature for each edge since temperatures are node-specific quantities. We obtain the network-wide energy flows by

$$\varphi = \frac{1}{2} Q \left(|\tilde{E}| - \tilde{E}\right)^\top x \tag{42}$$

where $|\tilde{E}|$ denotes the elementwise absolute value operator of $\tilde{E}$, i.e., $|\tilde{E}| = [|\tilde{E}_{ik}|]$, x is the vector of state variables defined as $x = [x_i]_{i\in\tilde{\mathcal{N}}}$, and Q is a diagonal matrix defined as $Q = \text{diag}(q_i)_{i\in\tilde{\mathcal{E}}}$. Subsequently, by multiplying φ with the full incidence matrix, we obtain the energy balance on each node. More precisely, we have

$$\phi = \tilde{E}\varphi \tag{43}$$

where $\phi \in \mathbb{R}^{|\tilde{\mathcal{N}}|}$ represents the nodal rate of change in energy due to in-flows and out-flows. By including external effects from heat exchangers and the environment, we can introduce the complete state-space description through the thermal dynamics of the network. To this end, given flow vector q, we define matrix $A(q)$ as follows:

$$A(q) = \frac{1}{2}\tilde{E} Q \left(|\tilde{E}| - \tilde{E}\right)^\top - D_\alpha \tag{44}$$

where D_α is the diagonal matrix of heat loss coefficients characterized as $D_\alpha = \text{diag}(\alpha_i)_{i\in\tilde{\mathcal{N}}}$. Also, let $\mathcal{W}$ be the set of nodes corresponding to heat exchangers in the network, i.e., $\mathcal{W} := \{i \in \tilde{\mathcal{N}} : w_i \neq 0\}$. Furthermore, we define a $|\tilde{\mathcal{N}}| \times |\mathcal{W}|$ matrix, denoted by B, with the entry in the ith row and jth column given by

$$B_{ij} = \begin{cases} \dfrac{1}{\rho c_p}, & \text{if } j = 1, \ldots, |\mathcal{W}| \text{and } i = i_j \\ 0, & \text{otherwise} \end{cases} \tag{45}$$

where $i_1, i_2, \ldots, i_{|\mathcal{W}|}$ are the elements of $\mathcal{W}$ sorted in an increasing order, i.e., $i_1 < i_2 < \cdots < i_{|\mathcal{W}|}$. Accordingly, the thermal dynamics of the network can be described by

$$\begin{aligned} V\dot{x} &= A(q)x + Bw \\ z &= Cx \end{aligned} \tag{P_{CT}}$$

where $V = \text{diag}(V_i)_{i\in\tilde{\mathcal{N}}}$ is the volume matrix, and $w = [w_i]_{i\in\mathcal{W}}$ is the vector of external inputs and disturbances. Note that $\mathcal{W}$ can be partitioned into disjoint subsets $\mathcal{W}_C$ and $\mathcal{W}_P$ to distinguish between consumer and producer interactions, respectively.

Remark 9: The volume matrix V is singular since $V_i = 0$ for $i \in \mathcal{N}$. One might suggest using a Schur decomposition to eliminate the algebraic equations associated with the network junctions. However, this approach requires inverting a submatrix of $A(q)$ and though $A(q)$ is diagonal and invertible, it depends on the control variable q, introducing nonlinear terms that significantly complicate the optimization problem. ◇

B. Time Discretization

A discrete-time model is required for the MPC problem. Due to the slow thermal dynamics of DHNs, online computational constraints, and demand measurement intervals, practical implementations typically use time steps τ_t ranging from 15 min to 1 h [18]. For explicit discretization schemes, satisfying the Courant-Friedichs-Lewy (CFL) condition, i.e., $q_i(k)\tau_t \leq V_i \ \forall i,\ k \in \mathbb{N}$, is difficult when modeling with large time steps. Hence, we employ the numerically stable implicit Euler method

$$x(k+1) = x(k) + \tau_t f_{\text{ct}}\left(x\left(k+1\right), u\left(k+1\right)\right) \tag{46}$$

where f_{ct} is the continuous-time dynamics. The application of the implicit Euler method to (P_{CT}) results in the following discrete-time system:

$$Vx(k+1) = Vx(k) + \tau_t\left[A(q(k))x(k+1) + Bw(k)\right] \tag{47}$$

or, equivalently, we can split the algebraic part from the equation by introducing a subset of variables $x^c(k) \in \mathbb{R}^{m_c}$ to denote the state of TN cells with positive volume and $x^j(k) \in \mathbb{R}^{|\mathcal{N}|}$ to denote the state of junctions with zero volume. As a result, we can describe the system through a discrete-time differential-algebraic equation (DAE) as follows:

$$\begin{aligned} x^c(k+1) &= f\left(x^c\left(k\right), x^j\left(k\right), u\left(k\right), d\left(k\right)\right) \\ 0 &= g\left(x^c\left(k\right), x^j\left(k\right), u\left(k\right), d\left(k\right)\right). \end{aligned} \tag{P_{DT}}$$

The system's dynamics are governed by the functions f and g, which relate the state vector $x(k) = \left[x^c(k)^\top \ x^j(k)^\top\right]^\top$, input vector $u(k) = \left[q_r(k)^\top \ P(k)^\top\right]^\top$, and disturbance $d(k)$. A description of these variables is detailed in Table I. Note that, in (P_{DT}), the previously mentioned external input $w(k)$ has been split into a controllable power injection part $P(k)$ considered in $u(k)$ and a disturbance part considered in $d(k)$, which represents the consumer demand.

TABLE I
DESCRIPTION OF SYSTEM VARIABLES

Symbol	Description	Dimension
$x^{\mathrm{c}}(k)$	State: Thermal node temperature	m_{c}
$x^{\mathrm{j}}(k)$	State: Junction temperature	$\lvert\mathcal{N}\rvert$
$q_r(k)$	Control input: Volume flow rate	m_r
$P(k)$	Control input: Power injection	$\lvert\mathcal{W}_P\rvert$
$d(k)$	Disturbance: Consumer demand	$\lvert\mathcal{W}_C\rvert$
$x(k)$	Combined state vector	$\lvert\tilde{\mathcal{N}}\rvert$
$u(k)$	Combined input vector	$m_r + \lvert\mathcal{W}_P\rvert$

V. ECONOMIC MPC FORMULATION FOR DHNS

In this section, we introduce our economic MPC scheme for optimizing the performance of DHNs. To this end, we formulate the MPC optimization problem, discuss the relevant design choices for the objective function, and present various computational techniques to improve the numerical performance of the employed solvers.

A. Problem Formulation

Consider the discrete-time dynamics ($\mathrm{P_{DT}}$). The receding horizon optimal control problem (OCP) at time k is defined as follows:

$$\begin{aligned}\min_{(x_t)_{t=1}^{N},(u_t)_{t=0}^{N-1}} \; & J_N\left((x_t)_{t=1}^{N},(u_t)_{t=0}^{N-1}\right)\\ \text{s.t. } & x_{t+1}^{c} = f\left(x_t^{c},x_t^{j},u_t,d_{t+k}\right)\\ & 0 = g\left(x_t^{c},x_t^{j},u_t,d_{t+k}\right)\\ & x_t \in \mathbb{X}_{t+k}\\ & u_t \in \mathbb{U}_{t+k}\\ & \forall t \in \{0,\dots,N-1\}\\ & x_0 = x(k)\end{aligned} \tag{OCP}$$

where $x(k)$ is the current state at time k, the sets $\mathbb{X}_t := \{x : \mathcal{F}_t(x) \le 0\}$ are time-varying constraint sets representing operational bounds on the state, and the sets $\mathbb{U}_t := \{u : \mathcal{H}_t(u) \le 0\}$ represent the time-varying operational constraints on the inputs, including the hydraulic constraints as defined in (11), (12), and (39) from Section III. Let the solution of the OCP for horizon N be denoted by $(x_{N,k}^{*}, u_{N,k}^{*})$, where the subscripts are included to stress the dependence of optimal solutions on N and k. In MPC, the optimal control problem in (OCP) is solved iteratively. In each step, the feedback control law is

$$(\mu_N)(x(k)) = u_0^{*}$$

where u_0^{*} is the first element of the optimal sequence $u_{N,k}^{*}$.

Remark 10: The OCP yields an optimal volume flow rate sequence, $q(k)$. However, direct actuation of valves by the high-level MPC is impractical. Therefore, $q(k)$ serves as a setpoint for a lower level valve controller. ◇

B. Objective Function

The objective function is a critical component in the design of economic MPC schemes, allowing for the selection of a cost function that accurately represents our practical goals or specifications. Given the current objective of optimizing the performance of the DHN, we define the objective function as follows:

$$J_N = J_N^{\mathrm{price}} + J_N^{\mathrm{temp}} + J_N^{\mathrm{diff}} + J_N^{\mathrm{sto}} + J_N^{\mathrm{slack}} \tag{48}$$

where each of these terms reflects a desirable operational feature or aspect, which are discussed as follows.

1) *Price Term:* The operational management requires minimization of operational costs. In addition, we assume that part of the generating mechanism is linked to a market, such as a heat pump purchased from the electricity grid. Hence, we use a linear cost function

$$J_N^{\mathrm{price}} = \sum_{t=0}^{N-1} R_t^{\mathrm{price}} P_t \tag{49}$$

where R_t^{price} represents the time-varying price, or relative price, of generating P_t.

2) *Temperature Term:* It is desired to operate DHNs at low temperatures to improve their efficiency. Therefore, we include a state term in the objective as follows:

$$J_N^{\mathrm{temp}} = \sum_{t=1}^{N} R_t^{\mathrm{temp}} x_t^{p} \tag{50}$$

with the penalty coefficient R_t^{temp} and power index $p \in \{1,2\}$ suggesting that the function can be linear or quadratic in x.

3) *Input Variation Term:* It is undesirable to have fast switching in supply temperatures in DHNs, primarily due to the pipeline deterioration from the resulting thermal stress [38]. Therefore, we consider a cost term as follows:

$$J_N^{\mathrm{diff}} = \sum_{t=0}^{N-2} R_t^{\mathrm{diff}} \left(P_{t+1} - P_t\right)^2 \tag{51}$$

which penalizes input deviations between any successive timesteps.

4) *Storage Term:* Minimization of operating costs and the temperature usually do not favor the charging of a storage buffer. Therefore, without any storage term, the MPC typically stays in the discharging mode for all of the storage units. To address this issue, we introduce a terminal tracking cost on the temperature of storage nodes as follows:

$$J_N^{\mathrm{sto}} = \left\| x_N^{\mathrm{sto}} - \bar{x}^{\mathrm{sto}} \right\|_{R^{\mathrm{sto}}}^2 \tag{52}$$

which is similar to the one employed in [28]. This term will encourage the MPC to charge situationally depending on the size of R^{sto}.

5) *Slack Term:* The optimization is a large-scale nonlinear program, where the dynamics and constraints change in each iteration due to time-varying elements. Accordingly, guaranteeing feasibility in every iteration is not

always possible. On the other hand, certain constraints, e.g., temperature bounds and demand satisfaction, may not be *hard* constraints, meaning that a certain degree of violation is allowed. For this, we introduce variables σ and a cost term as follows:

$$J_N^{\text{slack}} = \|\sigma\|^2_{R^{\text{slack}}} \tag{53}$$

with R^{slack} chosen to be large enough penalizing undesired constraint violations.

C. Improving Numerical Performance

The design of MPC algorithms, which inherently involve the iterative solution to an OCP, depends on the convergence speed of the numerical solvers used to obtain the solution. To this end, we implement various methods to improve the computational performance, as discussed in the following.

1) *Warm Starting:* This technique can improve computational speed by providing the numerical solver with a near-optimal initial guess. After a single iteration, we possess the N-step prediction of the state x. Thus, in the next iterate, we initialize the solver with $x_0^{k+1}, x_1^{k+1}, \ldots, x_{N-1}^{k+1} \leftarrow x_0^{k*}, x_1^{k*}, \ldots, x_{N-1}^{k*}$, where k denotes the index for the current iteration. This process is repeated for all subsequent iterations.
2) *Objective Terms:* Certain objective terms can assist the numerical solver in finding a solution. In particular, we noted that the input variation term (51) significantly improves the speed of convergence.

Other approaches to reduce complexity include implementing a *control horizon* or *move blocking*, which fix control inputs over certain time periods, but may lead to restrictive solutions, see [8], [39].

VI. Numerical Experiments and Results

In this section, to assess and verify the economic and computational performance of our proposed methods, we perform suitably designed numerical experiments and simulation studies. To this end, we compare the proposed method to existing control strategies in the literature, including single-producer MPCs (SP-MPC) algorithms, which are based on, or similar to, optimization-based controllers used in [18] and [28]. In addition, we compare with a rule-based control (RBC) scheme implementation, which is close to the widely adopted approach in practice for the control of DHNs. Furthermore, we perform a numerical study to evaluate the computational tractability of the proposed methods. In particular, we assess the impacts of spatial oversampling and changing the prediction horizon on the computational load and performance of the algorithms. The DHN considered in our numerical experiments is the AROMA network, introduced in Section II-D and illustrated in Fig. 6.

For our numerical experiments, we employ a standard laptop with an Intel i7-1185G7 processor to run the simulations and Julia creates the models. We use the mathematical programming package JuMP.jl [40] to build the optimization problems, Ipopt [41] to solve the problems, and DifferentialEquations.jl [42] to simulate the DHN between iterations.

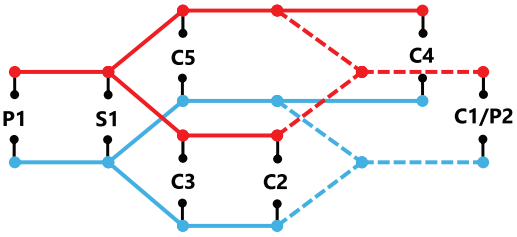

Fig. 6. AROMA network is labeled with five consumers (labeled C), two producers (labeled P), and a storage (labeled S). Dashed lines indicate pipes on which bidirectional flows are allowed.

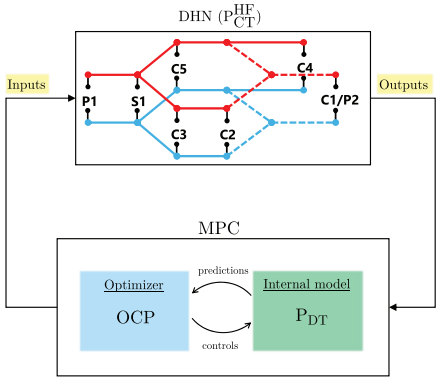

Fig. 7. MPC feedback loop.

Before proceeding with the results, we introduce the ground truth reference model to which we apply the generated inputs, and, second, we discuss the physical parameters, load profiles, and electricity price profiles that were used in all simulations.

A. High-Fidelity Model

To assess the performance of the controller, we will apply the inputs $\mu_N[x(k)]$ to a high-resolution simulator that accurately describes the system. This simulator model, called here the *high-fidelity model*, acts as a representation of the real system. In [36], a detailed study on the accuracy of these graph-theoretic simulation models for district heating systems is provided along with a comparison to the other high-fidelity simulators that have been verified using real measurements. It is shown in [36] that, even for reduced-order models, their method exhibits high accuracy.

We refer to the high-fidelity model by $P_{\text{CT}}^{\text{HF}}$, which is a continuous-time system obtained using the same method as in (P_{CT}). Nonetheless, the dimension of x^{HF}, the state vector in the high-fidelity model, is equal to $|\mathcal{N}|+\beta m_c$, where $\beta \in \mathbb{N}$, and $\tau_{x_i}^{\text{HF}} = \tau_{x_i}/\beta$ to compensate for pipe length. This change suggests that for large values of β, we achieve a much higher spatial resolution, which leads to a better approximation of the original system. Finally, the resulting system $P_{\text{CT}}^{\text{HF}}$ is a system of differential-algebraic equations that we solve using dedicated solvers in Julia [42]. In each iteration, the solver computes the evolution of the states for τ_t seconds. Every iteration is initialized using the final step of the previous simulation $x^{\text{HF}}(k\tau_t - \tau_t)$ and the optimal inputs $(\mu_N)(x(k))$ remain constant for the duration of the simulation, i.e., on

TABLE II
LIST OF PHYSICAL SYSTEM PARAMETERS

Parameter	Value	Units
T_a	10	°C
ρ	981	kg·m^{-3}
c_p	4182	J·kg^{-1}·K
U_{pipe}	0.4	W·m^{-2}· K^{-1}
K_{pipe}	0.02	-
d_{pipe}	70 - 107	mm
d_{sto}	2000	mm
L_{pipe}	300 - 600	m
L_{sto}	8	m

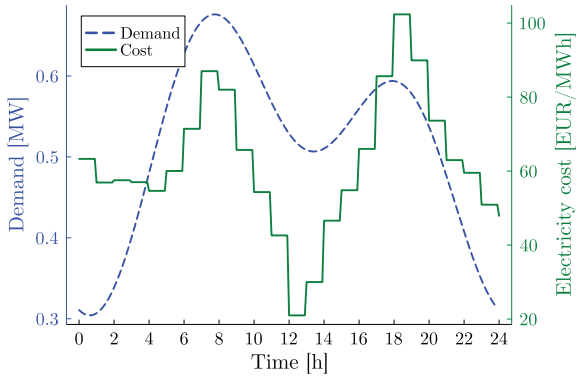

Fig. 8. Total demand profile and electricity price profile for 24 h. Electricity prices are from March 14, 2024, in The Netherlands.

TABLE III
FRACTION OF TOTAL DEMAND

C1/P2	C2	C3	C4	C5
0.08	0.34	0.11	0.08	0.38

the time interval $[k\tau_t - \tau_t, k\tau_t]$. After completion, the current state $x(k) = x^{\text{HF}}(k\tau_t)$ is fed into the MPC controller, see Fig. 7 for a diagram of this feedback loop.

B. Parameters and Data

In Table II, we list the physical parameters used in our simulations. System dimensions such as pipe diameters and lengths are the same as in [18]. We obtain the heat transmission coefficient U_{pipe} from [4, p. 77], and the friction coefficient K_{pipe} from [4, p. 444].

The demand profile employed here is an approximation of the one used in [18]. The electricity prices are acquired from Ember [43], where hourly electricity spot prices are provided for The Netherlands. We use price data from March 14, 2024, to determine the relative price term in (49), i.e., R_t^{price}. Fig. 8 illustrates the demand and electricity prices for 24 h, where only the net demand of consumers is shown. The demand of each individual consumer is computed as a fraction of the total demand as shown in Table III, assuming the same load distribution as in [18].

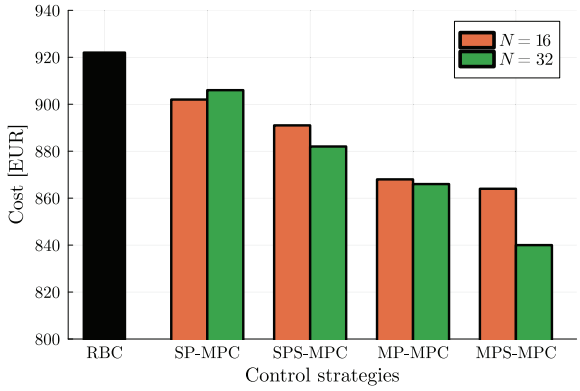

Fig. 9. Results of simulation 1. All results are based on 24 h of simulation. Results from left to right are for: RBC, SP-MPC, single-producer MPC with storage (SPS-MPC), multiproducer MPC (MP-MPC), and multiproducer MPC with storage (MPS-MPC). The average runtime for each iteration of the MPC algorithms was under 10 s.

C. Economic Performance and Comparisons

We conduct a comparative analysis of our proposed method against several established control strategies, including RBC and MPC for single-producer DHNs without storage capabilities. The existing RBC strategy is referred to as RBC, while the single-producer MPC strategy is denoted by SP-MPC. Our proposed methods are referred to as follows: the single-producer model with storage is denoted by SPS-MPC, the multiproducer model without storage is referred to as MP-MPC, and the multiproducer model with storage is indicated as MPS-MPC.

To quantify the economic value of the proposed methods, we analyze the financial implications for network operators under representative operating conditions. Here, prosumer C1/P2 generates a heat surplus of 100 kW during the interval 12:00–17:00, resulting in negative net demand. To maintain a similar total demand for comparative analysis, we introduce a compensatory 80 kW load increase at consumer C4.

1) Cost Comparison: In our numerical experiments, we set the control interval to $\Delta t = 15$ min. The cost function J_N is formulated to prioritize economic performance, with the relative price term R_t^{price} weighted substantially higher than other objective function terms, excluding slack variable penalties. A general overview of the economic performance results is presented in Fig. 9.

2) Quantifying the Effect of Slack Variables: To assess the true performance of the proposed methods, we quantify the extent to which the constraints have been violated as a consequence of the effects of the slack variables.

In our analysis, we observe distinct patterns in constraint violations. The pumping capacity bottlenecks manifest primarily as demand violations (DVs), where the network cannot deliver sufficient flow rates to meet consumer requirements. Conversely, temperature violations, defined as failures to maintain minimum required supply temperatures at consumer substations occur predominantly in scenarios where pumping capacity is sufficient to meet demand. While theoretical coupling between these constraint violations is possible, our simulations suggest they tend to be mutually exclusive, with

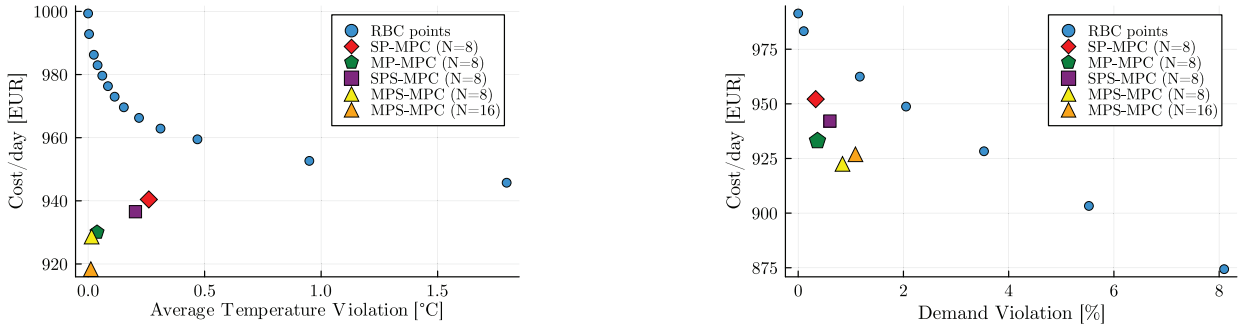

(a) (b)

Fig. 10. Relationship between operational costs and constraint violations under different pump configurations measured over a 4-day period. (a) Daily operating costs versus temperature violations for a DHN with sufficient pumping capacity. (b) Daily operating costs versus DVs for a DHN operating with pumping capacity constraints.

temperature violations emerging only when demand is fully satisfied and DVs occurring only under pumping capacity constraints.

Temperature requirements, typically mandated by regulatory frameworks, remain critical operational constraints that DHN operators must prioritize. For a simulation of t_f time steps, we quantify these average temperature violations (ATVs) in degrees Celsius as follows:

$$\text{ATV} = \frac{1}{t_f|\mathcal{W}_C|}\sum_{k=1}^{t_f}\sum_{c\in\mathcal{W}_C}\max\left(0, T_{\text{sup,min}} - T_c\,(k)\right). \tag{54}$$

On the other hand, network operators must ensure sufficient heat delivery to meet consumer demand requirements. We quantify DV over t_f steps as follows:

$$\text{DV} = 100\% \times \frac{\sum_{k=1}^{t_f}\sum_{j\in\mathcal{W}_C} d_j(k) - d_j^{\text{true}}(k)}{\sum_{k=1}^{t_f}\sum_{j\in\mathcal{W}_C} d_j(k)}$$

where the true heat exchange is defined as follows:

$$d_j^{\text{true}}(k) = q_j(k)\left(T_{j-1}(k) - T_j(k)\right), \quad j \in \mathcal{W}_C.$$

In Fig. 10, we compare these violation metrics against the operational costs obtained in each method.

Discussion: Several key observations emerge from Figs. 9 and 10. First, there is a noticeable improvement trend in cost reduction, with each feature added to the algorithm providing incremental benefits. The MPS-MPC algorithm with $N = 32$ achieves the highest performance, demonstrating an 9% cost reduction compared with the rule-based controller.

Our analysis of constraint violations reveals that the MPC-based approaches actively optimize network operations based on predicted demand and price signals, resulting in dynamic temperature management rather than simple static setpoint tracking. This continuous optimization allows the controller to systematically reduce average network temperatures when beneficial while maintaining required service levels, a capability that rule-based controllers inherently lack. This dynamic temperature management is key to achieve both cost reductions and improved constraint satisfaction compared to rule-based approaches.

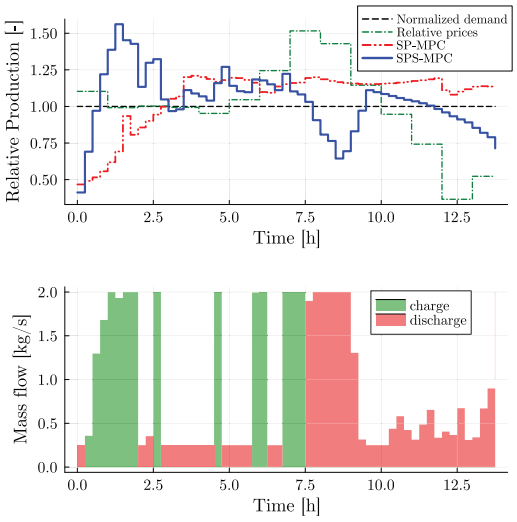

Fig. 11. Upper plot compares the power injection relative to demand extraction for both SP-MPC and SPS-MPC methods, with the normalized heat generation cost shown in green for reference. The lower plot illustrates the storage buffer's charging and discharging modes in SPS-MPC, maintaining zero net mass flow throughout the simulation period.

In addition, when analyzing DVs under pumping capacity constraints, the data suggest that prosumer-based control strategies, particularly MP-MPC and MPS-MPC, can better manage network limitations. The ability to actively coordinate multiple producers and redistribute flow patterns allows these approaches to excel at balancing competing objectives, demonstrating superior performance in maintaining service quality while optimizing operational costs.

D. Added Value of Storage

The aim of this section is to demonstrate the benefits of storage in the DHN. As can be seen from Fig. 9, the integration of storage yields significant economic benefits. In the top part of Fig. 11, the production schedules of the SP-MPC and SPS-MPC are plotted against each other. Second, the lower portion of the figure illustrates the corresponding storage charging and discharging periods. It is worth noting that, in this case, we

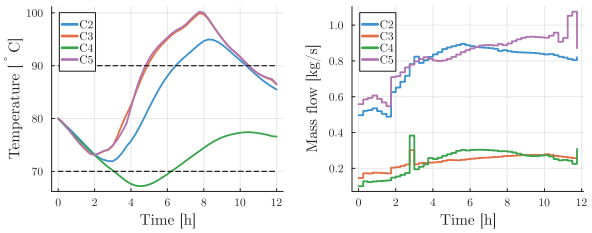

Fig. 12. Consumer inlet temperatures and mass flows for an SP-MPC case.

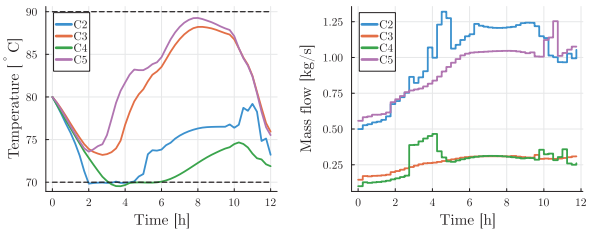

Fig. 13. Consumer inlet temperatures and mass flows for an MP-MPC case.

have additionally implemented a constraint that ensures that the total charging volume approximately matches the total discharging volume over the course of the day. Further specific details regarding this constraint are provided in the subsequent discussion.

Discussion: The results demonstrate that the controller effectively utilizes storage capacity to enable operational flexibility, as illustrated in Fig. 11. The comparison between SPS-MPC and SP-MPC reveals that the former shifts producer load by charging storage during early hours and discharging after approximately 7.5 h, thereby reducing producer load and achieving cost savings during high-price periods.

Several limitations should also be acknowledged. While the storage term in the cost function, introduced in Section V-B, aims to maintain adequate hot water levels in the top storage layer, its effectiveness is highly dependent on layer volumes and objective weight selection. Small weights lead to continuous discharge, while only substantially large weights induce charging behavior. Hence, in this study, we have opted to manually constrain the charging rates to ensure the total charging volume is equal to the discharging volume and emulate a more equal scenario.

E. Added Value of Multiple Producers

In addition to distributing heat production, which allows facilities like waste incineration plants or data centers to contribute to DHNs, multiple producers can reduce the pressure load on the central plant by dividing supply streams. Since pressure drop increases significantly with flow velocity, each pipeline has a limited flow capacity. Distributing heat supply flows among different producers enables higher mass flows at consumer stations, providing better operational margins. For this example, the setup has been modified in three ways. First, prosumer C1/P2 now acts as a full producer, consistently generating 100 kW of heat for the DHN, similar to a waste incineration plant or data center. Second, the available pumping power on each edge has been scaled down to emphasize hydraulic constraints. Third, temperature bounds are tightened to $70 \leq T \leq 90$ for all system states, with any values outside this range indicating the optimization could not find a feasible solution within these bounds.

In Fig. 12, the consumer temperatures and mass flows for the single-producer case are shown. On the other hand, Fig. 13 shows the temperatures and mass flows at consumers when C1/P2 contributes 100 kW constantly and P1 is freely controllable, corresponding to the multiproducer case.

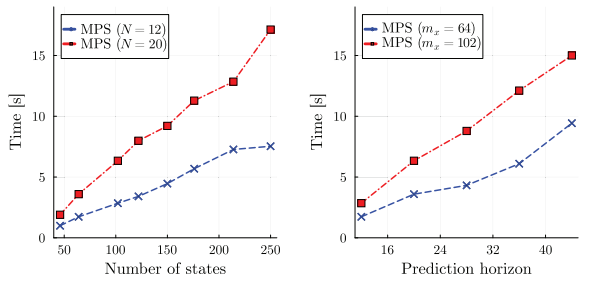

Fig. 14. *Median solver* times for the MPS-MPC algorithm using a prediction horizon $N = 12$ and $N = 20$ for different numbers of state variables (left). For two models, one with 64 states and one with 102 states, the *median solver* time based on the chosen prediction horizon (right).

Discussion: The results show that in the multiproducer scenario, the network is able to deliver more heat to large consumers C2 and C5. In particular, the peak flow rate of C2 in Fig. 13 lies about 40% higher than in Fig. 12. The increase can be attributed to the fact that C2 receives heat from both P1 and C1/P2 sources. Consequently, P1's contribution to C2 is reduced, enabling it to allocate a greater share of its flow to C5, the largest consumer. Overall, the aggregate energy requirement in the multi-producer scenario, comprising the combined outputs of P1 and C1/P2, is roughly equivalent to the total production of P1 in the single-producer scenario. Therefore, the MP-MPC shows improved performance compared to the SP-MPC in staying within operational limits and fairly distributing heat.

F. Computational Study

Finally, we examine the computational performance and scalability of our algorithms for various model resolutions and prediction horizons. In Fig. 14, the median computational times of the solver iterations for different model resolutions (left) and prediction horizons (right) are presented.

Discussion: In general, the computational cost associated with increasing model complexity remains manageable from an operational perspective, with even the most complex models requiring, on average, less than a minute per iteration. However, our observations indicate that the consistency of the solver in finding solutions within acceptable times diminishes under certain conditions, particularly for more complex models. These include models with over 200 states or with a prediction horizon greater than or equal to 40, where solution times can vary significantly.

Assuming the existence of a feasible solution, a pragmatic approach to deal with varying solver times involves constraining the number of solver iterations or the solver time to ensure that controls are computed within the required timeframe, even if this may result in a decrease in solution quality. Nonetheless, increasing model complexity does not necessarily enhance performance. In certain scenarios, reducing the model resolution can actually decrease model mismatch. This is due to the fact that truncation error is influenced by the CFL condition, and this error is minimized when the CFL value is close to 1 [36]. Consequently, the determination of model resolution is not straightforward and should be carefully considered on a case-by-case basis.

G. Limitations and Future Work

While our results demonstrate the effectiveness of MPC approaches for DHNs, several limitations should be acknowledged. The performance of the proposed methods relies on accurate demand predictions, with prediction errors affecting controller performance. Our implementation assumes that both perfect knowledge of system parameters and access to full-state measurements throughout the network. In practice, these assumptions may not hold, as many temperature and flow measurements might be unavailable or inaccurate. From a computational perspective, solution times increase with model complexity and prediction horizon length, which may impact scalability for larger networks. In addition, the nonconvex nature of the optimization problem, particularly from bidirectional flow constraints, can cause the solver to struggle in finding optimal trajectories. This sometimes requires warm-starting strategies to guide the optimization toward desired flow configurations, an approach that introduces additional implementation complexity. Future work could address these aspects through robust MPC formulations to handle demand uncertainty, state estimation techniques for networks with limited measurements, and the development of computationally efficient optimization strategies.

VII. Conclusion

We developed an economic MPC algorithm designed for the operational management of DHNs incorporating essential elements of 4th-generation DHNs such as multiple distributed heat sources, prosumers, and storage. A key aspect of our algorithm is its innovative treatment of hydraulic constraints through a convexification approach. We have conducted comprehensive numerical experiments to evaluate the proposed features, demonstrating that MPC approaches significantly outperformed conventional rule-based controllers, yielding up to 9% cost reduction alongside reduced constraint violations, with computation times remaining within practical limits. Furthermore, the integration of storage capabilities and multiple-producer configurations enhanced these performance metrics.

References

[1] ISO New England.(2024). *Final 2024 Heating Electrification Forecast*. [Online]. Available: https://www.iso-ne.com/static-assets/documents/100010/final-2024-heating-electrification-forecast.pdf

[2] Heat Roadmap Eur.(2017). *Heating and Cooling: Facts and Figures—The Transformation Towards a Low-carbon Heating & Cooling Sector*. [Online]. Available: https://www.heatroadmap.eu

[3] A. Battaglini, N. Komendantova, P. Brtnik, and A. Patt, "Perception of barriers for expansion of electricity grids in the European union," *Energy Policy*, vol. 47, pp. 254–259, Aug. 2012.

[4] S. Frederiksen and S. Werner, *District Heating and Cooling*. Lund, Sweden: Studentlitteratur AB, 2013.

[5] N. N. Novitsky et al., "Smarter smart district heating," *Proc. IEEE*, vol. 108, no. 9, pp. 1596–1611, Sep. 2020.

[6] H. Lund et al., "4th generation district heating (4GDH): Integrating smart thermal grids into future sustainable energy systems," *Energy*, vol. 68, pp. 1–11, Apr. 2014.

[7] A. Vandermeulen, B. van der Heijde, and L. Helsen, "Controlling district heating and cooling networks to unlock flexibility: A review," *Energy*, vol. 151, pp. 103–115, May 2018.

[8] M. Schwenzer, M. Ay, T. Bergs, and D. Abel, "Review on model predictive control: An engineering perspective," *Int. J. Adv. Manuf. Technol.*, vol. 117, nos. 5–6, pp. 1327–1349, 2021.

[9] C. De Persis and C. S. Kallesoe, "Pressure regulation in nonlinear hydraulic networks by positive and quantized controls," *IEEE Trans. Control Syst. Technol.*, vol. 19, no. 6, pp. 1371–1383, Nov. 2011.

[10] F. Strehle, J. E. Machado, M. Cucuzzella, A. J. Malan, S. Hohmann, and J. M. A. Scherpen, "A unifying passivity-based framework for pressure and volume flow rate control in district heating networks," *IEEE Trans. Control Syst. Technol.*, vol. 32, no. 4, pp. 1323–1340, Jul. 2024.

[11] J. Simonsson, K. T. Atta, and W. Birk, "Semi-decentralized temperature control in district heating systems," *J. Process Control*, vol. 140, Aug. 2024, Art. no. 103251.

[12] S. Ahmed, J. E. Machado, M. Cucuzzella, and J. M. A. Scherpen, "Control-oriented modeling and passivity analysis of thermal dynamics in a multi-producer district heating system," *IFAC-PapersOnLine*, vol. 56, no. 1, pp. 175–180, 2023.

[13] T. Scholten, C. De Persis, and P. Tesi, "Modeling and control of heat networks with storage: The single-producer multiple-consumer case," *IEEE Trans. Control Syst. Technol.*, vol. 25, no. 2, pp. 414–428, Mar. 2017.

[14] J. E. Machado, J. Ferguson, M. Cucuzzella, and J. M. A. Scherpen, "Decentralized temperature and storage volume control in multiproducer district heating," *IEEE Control Syst. Lett.*, vol. 7, pp. 413–418, 2023.

[15] J. E. Machado, M. Cucuzzella, and J. M. A. Scherpen, "Modeling and passivity properties of multi-producer district heating systems," *Automatica*, vol. 142, Aug. 2022, Art. no. 110397.

[16] A. Benonysson, B. Bøhm, and H. F. Ravn, "Operational optimization in a district heating system," *Energy Convers. Manage.*, vol. 36, no. 5, pp. 297–314, May 1995.

[17] H. Zhao, J. Holst, and L. Arvastson, "Optimal operation of coproduction with storage," *Energy*, vol. 23, no. 10, pp. 859–866, Oct. 1998.

[18] R. Krug, V. Mehrmann, and M. Schmidt, "Nonlinear optimization of district heating networks," *Optim. Eng.*, vol. 22, no. 2, pp. 783–819, Jun. 2021.

[19] F. Hante and M. Schmidt, "Complementarity-based nonlinear programming techniques for optimal mixing in gas networks," *EURO J. Comput. Optim.*, vol. 7, no. 3, pp. 299–323, Sep. 2019.

[20] G. Sandou, S. Font, S. Tebbani, A. Hiret, and C. Mondon, "Predictive control of a complex district heating network," in *Proc. 44th IEEE Conf. Decis. Control*, Sep. 2005, pp. 7372–7377.

[21] F. Verrilli et al., "Model predictive control-based optimal operations of district heating system with thermal energy storage and flexible loads," *IEEE Trans. Autom. Sci. Eng.*, vol. 14, no. 2, pp. 547–557, Apr. 2017.

[22] S. S. Farahani, Z. Lukszo, T. Keviczky, B. De Schutter, and R. M. Murray, "Robust model predictive control for an uncertain smart thermal grid," in *Proc. Eur. Control Conf. (ECC)*, Jun. 2016, pp. 1195–1200.

[23] D. Quaggiotto, J. Vivian, and A. Zarrella, "Management of a district heating network using model predictive control with and without thermal storage," *Optim. Eng.*, vol. 22, no. 3, pp. 1897–1919, Sep. 2021.

[24] J. Jansen, F. Jorissen, and L. Helsen, "Optimal control of a fourth generation district heating network using an integrated non-linear model predictive controller," *Appl. Thermal Eng.*, vol. 223, Mar. 2023, Art. no. 120030.

[25] J. Jansen, F. Jorissen, and L. Helsen, "Mixed-integer non-linear model predictive control of district heating networks," *Appl. Energy*, vol. 361, May 2024, Art. no. 122874.

[26] L. Frison, M. Kollmar, A. Oliva, A. Bürger, and M. Diehl, "Model predictive control of bidirectional heat transfer in prosumer-based solar district heating networks," *Appl. Energy*, vol. 358, Mar. 2024, Art. no. 122617.

[27] M. Rose, H. Gernandt, J. E. Machado, and J. Schiffer, "Model predictive control of district heating grids using stabilizing terminal ingredients," 2024, *arXiv:2404.01820*.
[28] A. La Bella, L. Nigro, and R. Scattolini, "Predictive control and benefit sharing in multi-energy systems," *IEEE Trans. Control Syst. Technol.*, vol. 32, no. 2, pp. 368–383, Mar. 2024.
[29] F. Agner, P. Kergus, R. Pates, and A. Rantzer, "Combating district heating bottlenecks using load control," *Smart Energy*, vol. 6, May 2022, Art. no. 100067.
[30] M. Sibeijn, S. Ahmed, M. Khosravi, and T. Keviczky, "Dissipativity analysis for economic nonlinear MPC of district heating networks," in *Proc. Eur. Control Conf. (ECC)*, Jun. 2024, pp. 1111–1118.
[31] A. J. Neale, R. F. Babus'Haq, S. D. Probert, and M. J. Shilston, "Thermal design of district-heating distribution networks," *Appl. Energy*, vol. 28, no. 4, pp. 269–282, Jan. 1987.
[32] S. El Mrabet, B. Lamrani, M. Abd-Lefdil, and T. Kousksou, "A brief overview of district heating pipe network progress," *Energy Convers. Manage., X*, vol. 23, Jul. 2024, Art. no. 100641.
[33] H. Dänschel, V. Mehrmann, M. Roland, and M. Schmidt, "Adaptive nonlinear optimization of district heating networks based on model and discretization catalogs," *SeMA J.*, vol. 81, no. 1, pp. 81–112, Mar. 2024.
[34] M. Rein, J. Mohring, T. Damm, and A. Klar, "Optimal control of district heating networks using a reduced order model," *Optim. Control Appl. Methods*, vol. 41, no. 4, pp. 1352–1370, Jul. 2020.
[35] D. B. West, *Introduction to Graph Theory*, vol. 2. Upper Saddle River, NJ, USA: Prentice-Hall, 2001.
[36] J. Simonsson, K. T. Atta, and W. Birk, "A graph theoretical approach to modeling of district energy networks," *IEEE Trans. Control Syst. Technol.*, vol. 32, no. 5, pp. 1616–1630, Sep. 2024.
[37] M. Sibeijn, S. Ahmed, M. Khosravi, and T. Keviczky, "Economic nonlinear model predictive control of prosumer district heating networks: The extended version," 2025, *arXiv:2501.17597*.
[38] S. van der Zwan and I. Pothof, "Operational optimization of district heating systems with temperature limited sources," *Energy Buildings*, vol. 226, Nov. 2020, Art. no. 110347.
[39] R. Gondhalekar and J.-I. Imura, "Least-restrictive move-blocking model predictive control," *Automatica*, vol. 46, no. 7, pp. 1234–1240, Jul. 2010.
[40] M. Lubin, O. Dowson, J. D. Garcia, J. Huchette, B. Legat, and J. P. Vielma, "JuMP 1.0: Recent improvements to a modeling language for mathematical optimization," *Math. Program. Comput.*, vol. 15, no. 3, pp. 581–589, Sep. 2023.
[41] A. Wächter and L. T. Biegler, "On the implementation of an interior-point filter line-search algorithm for large-scale nonlinear programming," *Math. Program.*, vol. 106, no. 1, pp. 25–57, Mar. 2006.
[42] C. Rackauckas and Q. Nie, "DifferentialEquations.Jl—A performant and feature-rich ecosystem for solving differential equations in Julia," *J. Open Res. Softw.*, vol. 5, no. 1, p. 15, May 2017.
[43] Sandbag Climate Campaign CIC.(2024). *European Wholesale Electricity Price Data*. [Online]. Available: https://ember-climate.org/data-catalogue/european-wholesale-electricity-price-data/

Max Sibeijn (Graduate Student Member, IEEE) received the B.Sc. degree in mechanical engineering and the M.Sc. degree in systems and control from Delft University of Technology, Delft, The Netherlands, in 2019 and 2021, respectively, where he is currently pursuing the Ph.D. degree with Delft Center for Systems and Control.

His research focuses on advanced topics within control theory and optimization, including nonlinear model predictive control, distributed optimization, learning value functions, sensor placement for partial differential equations (PDEs), and dissipativity for model predictive control. He is particularly interested in applying these concepts to large-scale networked systems, such as district heating networks.

Saeed Ahmed (Member, IEEE) received the Ph.D. degree from Bilkent University, Ankara, Turkey, in 2018.

During his Ph.D., he was a visiting Ph.D. scholar at the CentraleSupele, Gif-sur-Yvette, France. He is a Tenure-Track Assistant Professor of systems and control with the University of Groningen, Groningen, The Netherlands, where he is also with the Engineering and Technology Institute Groningen and the Jan C. Willems Center for Systems and Control. Prior to joining this position, he held postdoctoral positions at the University of Groningen and the Technical University of Kaiserslautern (now RPTU), Kaiserslautern, Germany. From a theoretical point of view, he is interested in stability and control, online optimization, observer design, nonlinear and hybrid (switched and impulsive) systems, dissipativity and passivity analysis, robust control, LPV systems, and time-delay systems. From an application point of view, he is interested in designing intelligent control algorithms for autonomous vehicles and district heating systems.

Dr. Ahmed received the Best Presentation Award in the control/robotics/communications/network category at the IEEE Graduate Research Conference 2018 held at Bilkent University. He also won the Outstanding Reviewer Award from the European Journal of Control. He is an Associate Editor of *Systems & Control Letters* and a member of the IFAC Technical Committees on Networked Systems, Non-Linear Control Systems, and Distributed Parameter Systems.

Mohammad Khosravi (Member, IEEE) received the B.Sc. degrees in electrical engineering and mathematical sciences from the Sharif University of Technology, Tehran, Iran, in 2011, the Postgraduate Diploma degree in mathematics from ICTP, Trieste, Italy, in 2012, the M.A.Sc. degree in electrical and computer engineering from Concordia University, Montreal, QC, Canada, in 2016, and the Ph.D. degree from the Swiss Federal Institute of Technology (ETH), Zürich, Switzerland, in 2022.

He was a Junior Research Scientist with the Mathematical Biology Group, Institute for Research in Fundamental Sciences, Iran, from 2012 to 2014. He is currently an Assistant Professor with Delft Center for Systems and Control (DCSC), Delft University of Technology, Delft, The Netherlands. His research interests involve data-driven and learning-based methods in modeling, model reduction, optimization, and control of dynamical systems and their applications in thermodynamics, buildings, energy, industry, and power systems.

Dr. Khosravi has won several awards, including the ETH Medal, the European Systems and Control Ph.D. Award, the Outstanding Student Paper Award in CDC 2020, the Outstanding Reviewer Award for IEEE JOURNAL OF CONTROL SYSTEMS LETTERS, and the Gold Medal of the National Mathematics Olympiad.

Tamás Keviczky (Senior Member, IEEE) received the M.Sc. degree in electrical engineering from Budapest University of Technology and Economics, Budapest, Hungary, in 2001, and the Ph.D. degree from the Control Science and Dynamical Systems Center, University of Minnesota, Minneapolis, MN, USA, in 2005.

He is currently a Professor with Delft Center for Systems and Control, Delft University of Technology, Delft, The Netherlands. He was a Post-Doctoral Scholar of control and dynamical systems with the California Institute of Technology, Pasadena, CA, USA. His research interests include distributed optimization and optimal control, model predictive control, and estimation of large-scale infrastructure systems, such as smart buildings, water, heat, and power networks. His research interests include distributed optimization and optimal control, model predictive control, and estimation of large-scale infrastructure systems, such as smart buildings, water, heat, and power networks.

Dr. Keviczky was a co-recipient of the AACC O. Hugo Schuck Best Paper Award for Practice in 2005. He has served as an Associate Editor for *Automatica* from 2011 to 2017 and for IEEE TRANSACTIONS ON AUTOMATIC CONTROL from 2021 to 2023.